Elasto-Static Modelling and Identification of a Deployable Cable-Driven Parallel Robot with Compliant Masts

Zane Zane, Stéphane Caro

Elasto-Static Modelling and Identification of a Deployable Cable-Driven Parallel Robot with Compliant Masts*

Zane Zaķe[1] and Stéphane Caro[2]

***Abstract*— Some cable-driven parallel robots (CDPRs) can be rapidly deployed on-site. To achieve such deployability, the fixed frame is usually substituted by four masts. However, not having any rigid fixture between the masts reduces the overall stiffness of the CDPR. This paper introduces a CDPR called Rocaspect, that has four compliant masts. The robot behavior and accuracy is evaluated experimentally and three different mast models are proposed.**

I. Introduction

Cable-driven parallel robots (CDPRs) are a subtype of parallel robots where rigid links are replaced by cables. Since cables are usually lightweight and the motors are typically mounted on the ground, therefore the only significant mass in motion is the moving-platform (MP), possibly with a payload. Due to this, CDPRs are being studied over increasing workspace sizes, for example: (a) IPAnema $8\,\text{m}\times 6\,\text{m}\times 5\,\text{m}$ [1]; (b) CoGiRo $16\,\text{m}\times 11\,\text{m}\times 6\,\text{m}$ [2]; (c) CDPR art installation Prince's Tears $20.8\,\text{m}\times 7.3\,\text{m}\times 5.1\,\text{m}$ [3]; Rocaspect deployed in a large configuration of $23.3\,\text{m}\times 19.0\,\text{m}\times 4.0\,\text{m}$ [4].

There are several ways to construct a CDPR. The stiffest option is to attach the CDPR pulleys directly to the building structure such as [2], [5], [6]. In this case it is reasonable to assume that the robot frame does not deform in any significant way and pulley coordinates remain the same throughout the use of such a CDPR. Attaching the pulleys to the building is not always feasible, therefore a rigid frame could be built. It generally has a rectangular cuboid shape such as in [7]–[9]. These types of CDPR structures are also usually assumed to be rigid. While there are some deployable CDPRs with a rectangular cuboid shape [7], [10], it is more convenient with respect to transportation and deployment to simply have free-standing masts such as in [11]–[14]. The drawback for such CDPRs is of course the reduced stiffness of the frame, since the masts are no longer interconnected.

There have been studies on CDPR stiffness that concentrated on quantifying the stiffness of the MP as a function of cable elasticity [6], [8], [15]–[17]. However, to our knowledge, the stiffness of the base structure itself and its effect on the MP pose errors has not been addressed except in [4].

Some efforts should be made to identify the parameters of the robot model and to determine the robot state when starting, namely to handle properly its initialization phase, for example, by performing some measurements with a Laser Tracker [1], [4]. However, if the robot structure deforms and the pulleys move due to the tension in the cables, the measured model does not match with the robot. During the experiments described in [4] it was observed that the masts are subject to torsion and bending due to their light structure, which greatly affected the MP accuracy. An initial mast model was proposed to explain the observed behavior. However, it was not possible to perform the identification of unknown parameters, such as the mast stiffness, at that stage. Thus, in this paper the compliance of Rocaspect masts is modelled, the unknown parameters are identified and the proposed model behavior is compared to the measured behavior. Ground truth measurements were performed using a Leica Absolute Laser Tracker AT901-MR (Leica LT) with a certified absolute accuracy of $\pm 15\,\mu\text{m}+6\,\mu\text{m/m}$ for a range of 40 m.

II. CDPR modelling

In this paper, a deployable CDPR named Rocaspect, shown in Fig. 1a, is presented. It has $n=4$ masts, and each of them is an assembly of multiple pieces, as shown in Fig. 1b. The metal beam is rigidified with three Dyneema shrouds of 6 mm in diameter. The MP is pulled by 8 cables.

TABLE I

Notation used throughout the paper

- $i=1,\ldots,n$ denotes the ith mast; there are $n=4$ masts.
- $j=1,\ldots,o$ denotes the jth cable; there are $o=2$ pulleys per mast.
- $r=1,\ldots,q$ denotes the rth shroud; there are $q=3$ shrouds per mast.
- Boldface lowercase characters denote vectors; boldface uppercase characters are matrices.
- $\mathscr{F}_\text{b}$, $\mathscr{F}_\text{mp}$, $\mathscr{F}_\text{be}$ denote the base, MP and beam frames respectively (resp.).
- ${}^\alpha\mathbf{T}_\beta=\begin{bmatrix}{}^\alpha\mathbf{R}_\beta & {}^\alpha\mathbf{t}_\beta\\ \mathbf{0}_3 & 1\end{bmatrix}$ is the homogeneous transformation matrix from $\mathscr{F}_\alpha$ to $\mathscr{F}_\beta$.
- $\mathbf{A}^{-1}$ and $\mathbf{A}^\dagger$ are the inverse and the pseudo-inverse of $\mathbf{A}$, resp.
- $[\mathbf{e}]_\times$ denotes the cross-product matrix of vector $\mathbf{e}$.
- ${}^\alpha\mathbf{a}$ is the vector $\mathbf{a}$ expressed in $\mathscr{F}_\alpha$
- subscript $(\bullet)_\text{b}$ denotes the base or world
- subscript $(\bullet)_\text{mp}$ denotes the MP
- subscript $(\bullet)_\theta$ denotes the three elastic joint model
- subscript $(\bullet)_\text{be}$ denotes the metal beam
- subscript $(\bullet)_\text{m}$ denotes the mast
- subscript $(\bullet)_\text{s}$ denotes the shroud
- subscript $(\bullet)_\text{p}$ denotes the passive stiffness
- subscript $(\bullet)_\text{a}$ denotes the active stiffness

*Supported by IRT Jules Verne (French Institute of Research and Technology in Advanced Manufacturing Technologies for Composite, Metallic and Hybrid Structures)

[1]Nantes Université, IRT Jules Verne, F-44000 Nantes, France, zane.zake@irt-jules-verne.fr

[2]Nantes Université, École Centrale Nantes, CNRS, LS2N, UMR 6004, F-44000 Nantes, France stephane.caro@ls2n.fr

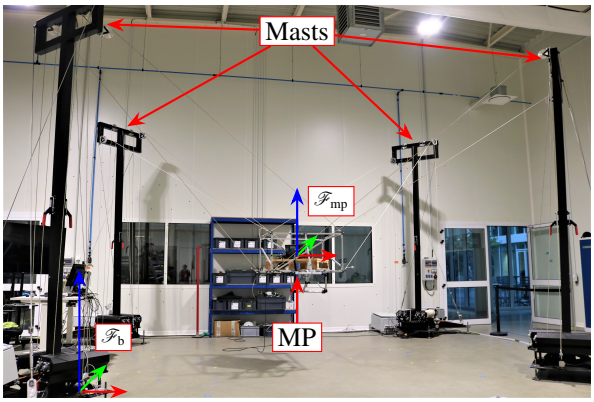

(a)

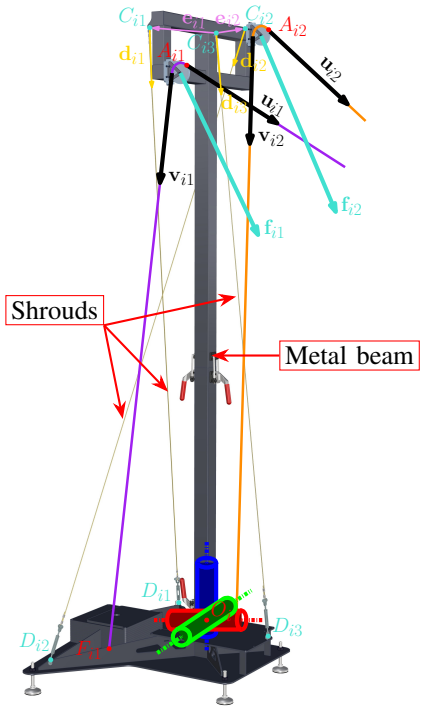

(b)

Fig. 1. Rocaspect: **(a)** test size of 8.3 m × 6.8 m × 4.0 m; **(b)** CAD model of the mast with: two cables (violet and orange); the resultant forces $\mathbf{f}_{ij}$; cable exit points A_{ij}; shroud upper and lower attachment points C_{ir} and D_{ir}, resp.; base point O_i; unit vectors $\mathbf{d}_{ir}$ along each shroud; vectors $\mathbf{e}_{ir}$ from C_{i3} (top point of the mast) to the remaining two upper attachment points; mast stiffness can be modelled as three one-DoF elastic joints at O_i

In the configuration shown in Fig. 1a, the CDPR size is 8.3 m × 6.8 m × 4.0 m with a footprint of 56.44 m^2. The MP size is 1.0 m × 1.0 m × 0.5 m and its mass is 50 kg. The masts are not fixed to the ground. To avoid them tipping over as a result of too high tensions in the CDPR cables, the maximum height the MP can attain is limited to 2 m.

Rocaspect has $o = 2$ cables per mast. The ijth cable vector of the ith mast is expressed as:

$$\mathbf{l}_{ij} = {}^{\text{b}}\mathbf{R}_{\text{mp}}\,{}^{\text{mp}}\mathbf{b}_{ij} + {}^{\text{b}}\mathbf{t}_{\text{mp}} - {}^{\text{b}}\mathbf{a}_{ij} \tag{1}$$

where ${}^{\text{b}}\mathbf{a}_{ij}$ is the Cartesian coordinates vector of cable exit point A_{ij} expressed in frame $\mathscr{F}_{\text{b}}$; ${}^{\text{mp}}\mathbf{b}_{ij}$ is the Cartesian coordinates vector of cable anchor point B_{ij} expressed in frame $\mathscr{F}_{\text{mp}}$; ${}^{\text{b}}\mathbf{t}_{\text{mp}}$ and ${}^{\text{b}}\mathbf{R}_{\text{mp}}$ are the position vector and rotation matrix of the MP expressed in the base frame $\mathscr{F}_{\text{b}}$.

The static equilibrium of the MP is given by:

$$\mathbf{W}\boldsymbol{\tau} + \mathbf{w}_{\text{g}} = 0 \tag{2}$$

where $\mathbf{w}_{\text{g}}$ is the MP gravity wrench, $\boldsymbol{\tau}$ is the cable tension vector, and $\mathbf{W}$ is the wrench matrix of the CDPR, defined as [18]:

$$\mathbf{W} = \begin{bmatrix} {}^{\text{b}}\mathbf{u}_{11} & \cdots & {}^{\text{b}}\mathbf{u}_{no} \\ {}^{\text{b}}\mathbf{R}_{\text{mp}}\,{}^{\text{mp}}\mathbf{b}_{11} \times {}^{\text{b}}\mathbf{u}_{11} & \cdots & {}^{\text{b}}\mathbf{R}_{\text{mp}}\,{}^{\text{mp}}\mathbf{b}_{no} \times {}^{\text{b}}\mathbf{u}_{no} \end{bmatrix} \tag{3}$$

where ${}^{\text{b}}\mathbf{u}_{ij}$ is the unit vector of $\mathbf{l}_{ij}$, namely ${}^{\text{b}}\mathbf{u}_{ij} = \frac{\mathbf{l}_{ij}}{||\mathbf{l}_{ij}||_2}$.

The pulleys on Rocaspect have a non-negligible size, thus pulley kinematics are taken into account in the control scheme, but not detailed here due to the limited space. Please refer to [6], [9], [19]–[21] for the expression of the unit vector ${}^{\text{b}}\mathbf{u}_{ij}$.

III. Modelling of the Rocaspect Masts

As described in [4], having a light mast structure can unfortunately lead to significant cable exit point displacement, especially if shroud tensions are not well managed. Consequently, since the cable exit point coordinates no longer correspond to the nominal ones, the accuracy of the MP is negatively affected. In this section several models are proposed to describe the mast top displacement. Note that throughout the paper when referring to *beam* only the metal beam is considered; and when referring to *mast* the assembly of the metal beam and shrouds is considered.

A. Three joint model (3R model)

Here, a slightly simplified version of the model proposed in [4] is presented. The mast shown in Fig. 1b can be modelled as an ideal infinitely rigid beam with three perpendicular and intersecting elastic joints at its base. Thus, the displacement $\delta\mathbf{c}_{i3}$ of the top of the ith mast C_{i3} due to the resultant wrench $\delta\mathbf{w}_i$ is described as:

$$\delta\mathbf{c}_{i3} = \mathbf{C}_{\theta i}\delta\mathbf{w}_i \tag{4}$$

where $\mathbf{C}_{\theta i}$ is the Compliance matrix, which is expressed as:

$$\mathbf{C}_{\theta i} = \mathbf{J}_i\mathbf{K}_{\theta i}^{-1}\mathbf{J}_i^T \tag{5}$$

$\mathbf{J}_i$ is the mast Jacobian matrix expressed for the top of the mast C_{i3} as follows:

$$\mathbf{J}_i = \begin{bmatrix} \overrightarrow{O_iC_{i3}} \times \mathbf{i} & \overrightarrow{O_iC_{i3}} \times \mathbf{j} & \overrightarrow{O_iC_{i3}} \times \mathbf{k} \\ \mathbf{i} & \mathbf{j} & \mathbf{k} \end{bmatrix} \tag{6}$$

with $\mathbf{i}$, $\mathbf{j}$ and $\mathbf{k}$ being the unit vectors along $\mathbf{x}_{\text{b}}$, $\mathbf{y}_{\text{b}}$, and $\mathbf{z}_{\text{b}}$ axes, resp., of the base frame $\mathscr{F}_{\text{b}}$ shown in Fig. 1a. O_i is the bottom of the mast, as depicted in Fig. 1b. The matrix $\mathbf{K}_{\theta i}$ is the (3×3) diagonal joint stiffness matrix of the ith mast.

The resultant wrench $\delta\mathbf{w}_i$ is defined as:

$$\delta\mathbf{w}_i = \begin{bmatrix} \mathbf{f}_i \\ \mathbf{m}_i \end{bmatrix} = \begin{bmatrix} \sum_{z=1}^{o} \mathbf{f}_{iz} \\ \sum_{z=1}^{o} ({}^{\text{b}}\mathbf{a}_{iz} - {}^{\text{b}}\mathbf{c}_{i3}) \times \mathbf{f}_{iz} \end{bmatrix} \tag{7}$$

with $\mathbf{f}_{ij} = \tau_{ij}(\mathbf{v}_{ij} + \mathbf{u}_{ij})$, $\mathbf{v}_{ij}$ is the unit vector of $\overrightarrow{A_{ij}F_{ij}}$. The displacement $\delta\mathbf{c}_{i3}$ is a (6×1) vector, where the first

three components define the translational displacement vector $\delta\mathbf{c}_{\mathrm{T}i3}$ of point C_{i3} and the last three components are those of the rotation displacement vector $\delta\mathbf{c}_{\mathrm{R}i3}$ of the mast top.

B. Beam Model

The beam used in this assembly is a straight hollow metal beam with a square cross-section, as shown in Fig. 2. Since it is fixed only on the bottom and forces are applied to it on the top, it can be modelled as a simple cantilever beam. The compliance matrix of such a beam is defined as [22]–[24]:

$$\mathbf{C}_{\mathrm{be}} = \begin{bmatrix} \frac{L}{EA} & 0 & 0 & 0 & 0 & 0 \\ 0 & \frac{L^3}{3EI_z} & 0 & 0 & 0 & \frac{L^2}{2EI_z} \\ 0 & 0 & \frac{L^3}{3EI_y} & 0 & -\frac{L^2}{2EI_y} & 0 \\ 0 & 0 & 0 & \frac{L}{GJ} & 0 & 0 \\ 0 & 0 & -\frac{L^2}{2EI_y} & 0 & \frac{L}{EI_y} & 0 \\ 0 & \frac{L^2}{2EI_z} & 0 & 0 & 0 & \frac{L}{EI_z} \end{bmatrix} \tag{8}$$

where E is the Young's modulus, G is the shear modulus, A is the cross-sectional area, L is the length of the beam, I_y and I_z are components of the moment of inertia $\mathbf{I}$; J is the polar moment of inertia. Given the shape of the beam shown in Fig. 2, the following equations are used:

$$I_y = I_z = \frac{s_{out}^4}{12} - \frac{s_{in}^4}{12} \tag{9}$$

$$J = \frac{s_{out} L (s_{out}^2 + L^2)}{12} \tag{10}$$

$$A = s_{out}^2 - s_{in}^2 \tag{11}$$

where s_{out} is the beam width, s_{in} is the hollow width.

Matrix $\mathbf{C}_{\mathrm{be}}$ is expressed in the beam frame $\mathscr{F}_{\mathrm{be}}$, where the beam is aligned with the $\mathbf{x}_{\mathrm{be}}$ axis. To express it in the world frame $\mathscr{F}_{\mathrm{b}}$, an augmented rotation matrix ${}^{\mathrm{b}}\mathbf{R}_{\mathrm{be}}^{aug}$ is defined in the following way:

$${}^{\mathrm{b}}\mathbf{R}_{\mathrm{be}}^{aug} = \begin{bmatrix} {}^{\mathrm{b}}\mathbf{R}_{\mathrm{be}} & \mathbf{0}_3 \\ \mathbf{0}_3 & {}^{\mathrm{b}}\mathbf{R}_{\mathrm{be}} \end{bmatrix} \tag{12}$$

where

$${}^{\mathrm{b}}\mathbf{R}_{\mathrm{be}} = \begin{bmatrix} 0 & 0 & -1 \\ 0 & 1 & 0 \\ 1 & 0 & 0 \end{bmatrix} \tag{13}$$

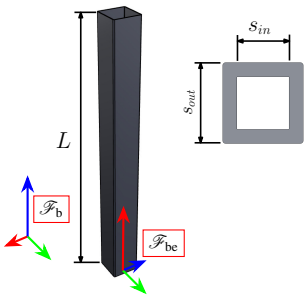

Fig. 2. Metal beam

The compliance matrix of the ith beam can then be expressed in $\mathscr{F}_{\mathrm{b}}$:

$$\mathbf{C}_{\mathrm{b}i} = {}^{\mathrm{b}}\mathbf{R}_{\mathrm{be}}^{aug} \mathbf{C}_{\mathrm{be}} {}^{\mathrm{be}}\mathbf{R}_{\mathrm{b}}^{aug} \tag{14}$$

and the displacement $\delta\mathbf{c}_{i3}$ due to the resultant wrench $\delta\mathbf{w}_i$ is defined as:

$$\delta\mathbf{c}_{i3} = \mathbf{C}_{\mathrm{b}i} \delta\mathbf{w}_i \tag{15}$$

C. Complete Mast Model

In this section, the complete mast model is proposed. As represented in Fig. 3, each mast is like a parallel robot on its own with four *legs*, where three *legs* are the shrouds and one *leg* is the metal beam. The displacement $\delta\mathbf{c}_{i3}$ of the top of the ith mast C_{i3} due to the resultant wrench $\delta\mathbf{w}_i$ is now defined as:

$$\delta\mathbf{c}_{i3} = \mathbf{K}_{\mathrm{m}i}^{\dagger} \delta\mathbf{w}_i \tag{16}$$

where $\mathbf{K}_{\mathrm{m}i}^{\dagger}$ is the pseudo-inverse of the mast stiffness matrix $\mathbf{K}_{\mathrm{m}i}$, which takes into account the stiffness of shrouds and the metal beam. For a parallel arrangement such as in Fig. 3, the total stiffness of the mast $\mathbf{K}_{\mathrm{m}i}$ is simply the sum of the leg stiffness matrices $\mathbf{K}_{il}$ [24]:

$$\mathbf{K}_{\mathrm{m}i} = \sum_{l=1}^{4} \mathbf{K}_{il} \tag{17}$$

The fourth leg is the beam defined in Section III-B. Its corresponding stiffness matrix takes the form:

$$\mathbf{K}_{i4} = \mathbf{C}_{\mathrm{b}i}^{-1} \tag{18}$$

The other three legs are shrouds and can be considered as a CDPR, for which the elasto-static modelling is described in [6], [8], [15]. The relationship between the mast top displacement and the wrench exerted on it is thus defined as:

$$\delta\mathbf{w}_i = \mathbf{K}_{\mathrm{s}i} \delta\mathbf{c}_{i3} \tag{19}$$

where $\mathbf{K}_{\mathrm{s}i}$ is the stiffness matrix of the three shroud system.

The static equilibrium for the mast top C_{i3} is defined as:

$$\mathbf{W}_{\mathrm{s}i} \boldsymbol{\tau}_{\mathrm{s}i} + \delta\mathbf{w}_i = 0 \tag{20}$$

where $\boldsymbol{\tau}_{\mathrm{s}i}$ is the shroud tension vector and $\mathbf{W}_{\mathrm{s}i}$ is the shroud wrench matrix defined as:

$$\mathbf{W}_{\mathrm{s}i} = \begin{bmatrix} {}^{\mathrm{b}}\mathbf{d}_{i1} & \dots & {}^{\mathrm{b}}\mathbf{d}_{iq} \\ {}^{\mathrm{b}}\mathbf{e}_{i1} \times {}^{\mathrm{b}}\mathbf{d}_{i1} & \dots & {}^{\mathrm{b}}\mathbf{e}_{iq} \times {}^{\mathrm{b}}\mathbf{d}_{iq} \end{bmatrix} \tag{21}$$

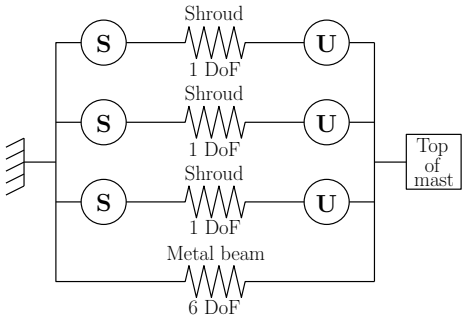

Fig. 3. Schematic of the mast taking into account the three shrouds and the metal beam. S and U stand for spherical and universal joints, resp.

where ${}^{\mathrm{b}}\mathbf{e}_{ir}$ is a vector pointing from point C_{i3} to the shroud attachment points C_{ir}; and ${}^{\mathrm{b}}\mathbf{d}_{ir}$ is the unit vector of each shroud as shown in Fig. 1b.

$\mathbf{K}_{\mathrm{s}i}$ can be expressed from (19) using (20) as:

$$\mathbf{K}_{\mathrm{s}i} = -\frac{\partial(\mathbf{W}_{\mathrm{s}i}\boldsymbol{\tau}_{\mathrm{s}i})}{\partial \mathbf{c}_{i3}} = -\frac{\partial \mathbf{W}_{\mathrm{s}i}}{\partial \mathbf{c}_{i3}}\boldsymbol{\tau}_{\mathrm{s}i} - \mathbf{W}_{\mathrm{s}i}\frac{\partial \boldsymbol{\tau}_{\mathrm{s}i}}{\partial \mathbf{c}_{i3}} = \mathbf{K}_{\mathrm{a}i} + \mathbf{K}_{\mathrm{p}i} \tag{22}$$

Thus, the stiffness matrix $\mathbf{K}_{\mathrm{s}i}$ consists of two parts $\mathbf{K}_{\mathrm{a}i}$ and $\mathbf{K}_{\mathrm{p}i}$. The former is usually named active or controllable stiffness, because it depends on the tensions in the shrouds. The latter is named passive or inherent stiffness, because it depends on the cable elasticity (Young's modulus). Note that $\mathbf{K}_{\mathrm{s}i}$ depends on the shroud tensions, therefore additional tension sensors are required to use this model.

Shroud elasticity is modelled according to the linear spring model so that:

$$\boldsymbol{\tau}_{\mathrm{s}i} = \mathbf{K}_{\mathrm{k}i}\delta\mathbf{l}_{\mathrm{s}i} \tag{23}$$

where $\mathbf{K}_{\mathrm{k}i}$ is a diagonal matrix containing the elastic coefficients k_{ir} for each shroud, $\delta\mathbf{l}_{\mathrm{s}i}$ is the vector of shroud length variations. Using (21) and (23), the passive stiffness $\mathbf{K}_{\mathrm{p}i}$ takes the following form:

$$\begin{aligned}\mathbf{K}_{\mathrm{p}i} = &-\mathbf{W}_{\mathrm{s}i}\mathbf{K}_{\mathrm{k}i}\frac{\partial \mathbf{l}_{\mathrm{s}i}}{\partial \mathbf{c}_{i3}} = \mathbf{W}_{\mathrm{s}i}\mathbf{K}_{\mathrm{k}i}\mathbf{W}_{\mathrm{s}i}^{T} = \\ &\sum_{r=1}^{q} k_{ir}\begin{pmatrix}\mathbf{D}_{ir} & \mathbf{D}_{ir}[\mathbf{e}_{ir}]_{\times}^{T} \\ [\mathbf{e}_{ir}]_{\times}\mathbf{D}_{ir} & [\mathbf{e}_{ir}]_{\times}\mathbf{D}_{ir}[\mathbf{e}_{ir}]_{\times}^{T}\end{pmatrix}\end{aligned} \tag{24}$$

with $\mathbf{D}_{ir} = {}^{\mathrm{b}}\mathbf{d}_{ir}\,{}^{\mathrm{b}}\mathbf{d}_{ir}^{T}$.

It was shown in [6] that Dyneema ropes have a progressive spring characteristic. That is, the elastic coefficients k_{ir} are not constant, but instead depend on the tension in the ropes and can be modelled as a polynomial of a second degree:

$$k_{ir} = \frac{k_{0ir} + k_{1ir}\tau_{\mathrm{s}ir} + k_{2ir}\tau_{\mathrm{s}ir}^{2}}{l_{\mathrm{s}ir}} \tag{25}$$

Active stiffness can be written as [8]:

$$\mathbf{K}_{\mathrm{a}i} = -\sum_{r=1}^{q}\frac{\tau_{\mathrm{s}ir}}{l_{\mathrm{s}ir}}\begin{pmatrix}-\mathbf{E}_{ir} & \mathbf{E}_{ir}[\mathbf{e}_{ir}]_{\times} \\ -[\mathbf{e}_{ir}]_{\times}\mathbf{E}_{ir} & \left[l_{\mathrm{s}ir}[{}^{\mathrm{b}}\mathbf{d}_{ir}]_{\times} + [\mathbf{e}_{ir}]_{\times}\mathbf{E}_{ir}\right][\mathbf{e}_{ir}]_{\times}\end{pmatrix} \tag{26}$$

with $\mathbf{E}_{ir} = \mathbf{I}_3 - \mathbf{D}_{ir}$ and $\mathbf{I}_3$ is the (3×3) identity matrix.

IV. Identification

In this section the identification of the unknown parameters necessary for the proposed models is presented.

A. Shroud elasticity

To determine the elasticity of the Dyneema shrouds, a new unused shroud was installed on a test bench shown in Fig. 4b. The length of the shroud between its winding grips was 0.5 m. The load is increased by tightening the nut on a threaded rod. A small plate attached to the shroud at 0.5 m mark changes its height as the shroud elongates due to the load and pushes on the needle of the digital indicator, which then measures the elongation. The pulling force was repeatedly increased and decreased as shown in Fig. 4a. Two sets of measurements were performed: from 50 kg to 400 kg (blue curves) and from 0 kg to 300 kg (green curves). Firstly, there is a significant difference between loading (solid curve) and unloading (dashed curve) the shroud. Secondly, the average curve is not a straight line, but indeed a polynomial curve. Thus, as discussed in [6], the Dyneema ropes appear to have a non-linear spring characteristic.

Using the recorded measurements, it is possible to identify the stiffness coefficients defined in (25). To do that, let the stiffness coefficients be the components of a vector $\mathbf{x}_{\mathrm{s}}$ so that $\mathbf{x}_{\mathrm{s}} = [k_0\ k_1\ k_2]$. Then the relation between the applied force and the shroud elongation can be obtained from (23) and (25) as:

$$\mathbf{A}_{\mathrm{s}e}\mathbf{x}_{\mathrm{s}} = b_{\mathrm{s}e} \tag{27}$$

where $\mathbf{A}_{\mathrm{s}e} = 1/l_0[\delta l_{\mathrm{s}e}\ \ \tau_{\mathrm{s}e}\delta l_{\mathrm{s}e}\ \ \tau_{\mathrm{s}e}^2\delta l_{\mathrm{s}e}]$, $b_{\mathrm{s}e} = \tau_{\mathrm{s}e}$, $l_{\mathrm{s}0} = 0.5$ m is the initial length of the shroud, and $\delta l_{\mathrm{s}e}$ and $\tau_{\mathrm{s}e}$ are the eth elongation and force measurement.

$\mathbf{A}_{\mathrm{s}e}$ and $b_{\mathrm{s}e}$ are concatenated into $\mathbf{A}_{\mathrm{s}}$ and $\mathbf{b}_{\mathrm{s}}$, resp. Then $\mathbf{x}_{\mathrm{s}}$ is obtained by minimizing the residual of the equation system $\mathbf{A}_{\mathrm{s}}\mathbf{x}_{\mathrm{s}} = \mathbf{b}_{\mathrm{s}}$ and it is $\mathbf{x}_{\mathrm{s}} = [935353.664;\ 144.320;\ -0.000465]$.

As can be seen in Fig. 4a, the obtained polynomial model

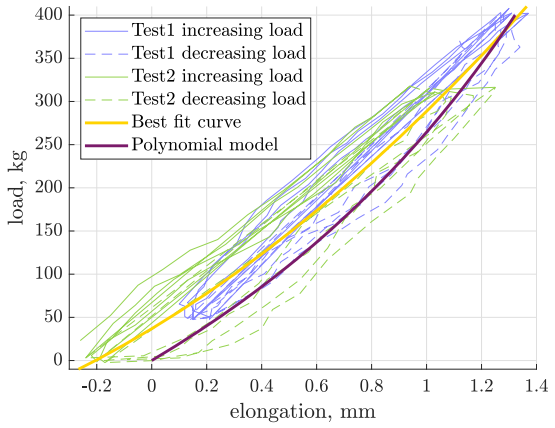

(a)

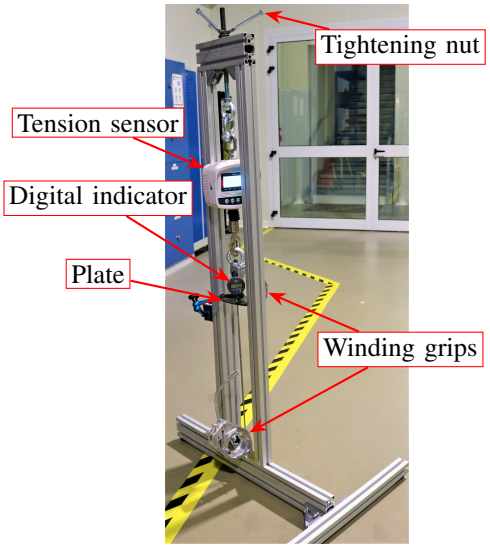

(b)

Fig. 4. Cable tensile test bench: **(a)** two measurement sets, the average curve and the polynomial model; **(b)** test bench

must pass through $(0,0)$, which does not correspond exactly to the average curve. Indeed, possibly another definition of the nonlinear spring characteristic could be envisaged such as in [25], [26], where the hysteresis is also taken into account.

B. Mast Model Identification

To identify the stiffness coefficients for each of the models, multiple experiments were done by varying the parameters shown in Table II. Shroud pretension was set while the MP was on a support. Then the MP was lifted by the CDPR to the initial pose ${}^b\mathbf{p}_p = [2.65\,\text{m};\ 2.5\,\text{m};\ 1.6\,\text{m};\ 0°;\ 0°;\ 0°]$ and the cable exit point A_{ij} coordinates were measured by Leica LT. Then the trajectory shown in Fig. 5a was executed multiple times per experiment, while measuring the displacement of mast 1 and then the displacement of the MP. As can be seen in Fig. 5b, there is a large difference of mast top C_{13} coordinates along $\mathbf{x}_\text{b}$ and $\mathbf{y}_\text{b}$ depending on the pretension in the shrouds. Furthermore, no matter the pretension, the point C_{13} moves, however the trajectory is almost identical for 1200 N and 800 N pretension, and still very similar with 400 N pretension. Likewise, changing the mass of the MP slightly affects mast top position and trajectory.

1) 3R Model Identification: In this model the unknowns are the diagonal elements of matrix $\mathbf{K}_{\theta i}$. Equation (4) can be rewritten using (5) as:

$$\mathbf{A}_{\theta e}\mathbf{x}_\theta = \mathbf{b}_{\theta e} \tag{28}$$

where $\mathbf{x}_\theta = [k_{\theta 1}\ \ k_{\theta 2}\ \ k_{\theta 3}]$ is the vector of joint stiffness coefficients; $\mathbf{b}_{\theta e} = \delta\mathbf{c}_{i3}$ and

$$\mathbf{A}_{\theta e} = \begin{bmatrix} J_{i11}\sum_{\alpha=1}^{6} J_{i\alpha 1}\delta w_{i\alpha} & \cdots & J_{i13}\sum_{\alpha=1}^{6} J_{i\alpha 3}\delta w_{i\alpha} \\ \vdots & \ddots & \vdots \\ J_{i61}\sum_{\alpha=1}^{6} J_{i\alpha 1}\delta w_{i\alpha} & \cdots & J_{i63}\sum_{\alpha=1}^{6} J_{i\alpha 3}\delta w_{i\alpha} \end{bmatrix} \tag{29}$$

where $J_{i11}\ldots J_{i63}$ are the components of $\mathbf{J}_i$, and $\delta w_{i\alpha}$ is the αth component of $\delta\mathbf{w}_i$.

Matrix $\mathbf{A}_{\theta e}$ and vector $\mathbf{b}_{\theta e}$ is filled for each eth point of the trajectory shown in Fig. 5 and then concatenated into $\mathbf{A}_\theta$ and $\mathbf{b}_\theta$, resp. Finally, the equation $\mathbf{A}_\theta\mathbf{x}_\theta = \mathbf{b}_\theta$ is solved for $\mathbf{x}_\theta$. Note that mast stiffness determined with this model is constant and does not take into account the variation of pretension in shrouds. Thus, the identification was done separately for each pretension shown in Table II and the results are shown in Table III. The obtained $k_{\theta 3}$ values were negative in most experiments, hence it is concluded that the mast is not twisting and those values are not meaningful.

TABLE II

PARAMETERS CHANGED DURING TESTS

Test Nr.	**MP mass**, kg	**Shroud pretension**, N	**Masts**
1 and 2	50 and 24	1200	mast 1
3	50	800	mast 1
4	50	400	mast 1
5 and 6	50 and 24	0 (slack shrouds)	mast 1
7	50	shrouds detached	mast 1
8	50	1200	all
9	50	0 (slack shrouds)	all
10	50	shrouds detached	all

2) Beam Model Identification: The known values are: $L = 3.651$ m, $s_{out} = 0.1$ m, $s_{in} = 0.094$ m. Young modulus E and shear modulus G are assumed to be unknown. Equation (15) is expressed in the form $\mathbf{A}_{\text{be}e}\mathbf{x}_\text{be} = \mathbf{b}_{\text{be}e}$, where $\mathbf{A}_{\text{be}e}$ takes the following form:

$$\mathbf{A}_{\text{be}e} = \begin{bmatrix} \frac{L^3}{3I_y}\delta w_{i1} + \frac{L^2}{2I_y}\delta w_{i5} & 0 \\ \frac{L^3}{3I_z}\delta w_{i2} + \frac{L^2}{2I_z}\delta w_{i4} & 0 \\ \frac{L}{A}\delta w_{i3} & 0 \\ -\frac{L^2}{2I_z}\delta w_{i2} + \frac{L}{I_z}\delta w_{i4} & 0 \\ \frac{L^2}{2I_y}\delta w_{i1} + \frac{L}{I_y}\delta w_{i5} & 0 \\ 0 & \frac{L}{J}\delta w_{i6} \end{bmatrix} \tag{30}$$

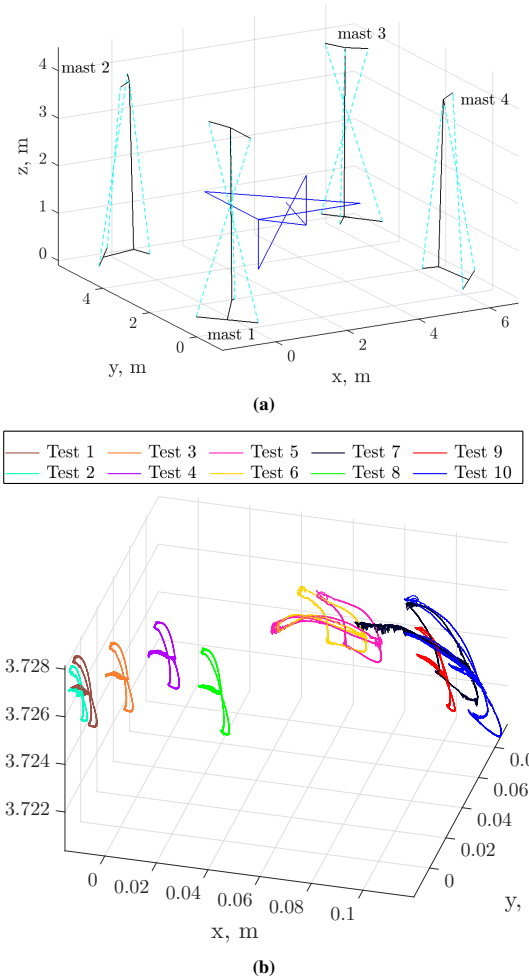

(a)

(b)

Fig. 5. Trajectories: **(a)** trajectory of the MP; **(b)** trajectory of the top of mast 1 depending on shroud tensions

TABLE III

IDENTIFIED STIFFNESS MATRIX $\mathbf{K}_{\theta i}$ ELEMENTS

Test Nr.	$k_{\theta 1}$, N/m	$k_{\theta 2}$, N/m	**Test Nr.**	$k_{\theta 1}$, N/m	$k_{\theta 2}$, N/m
1 and 8	271430	230527	2	260912	248326
3	243201	237652	4	219668	218580
5 and 9	51224	52847	6	42110	56700
7 and 10	75562	63079			

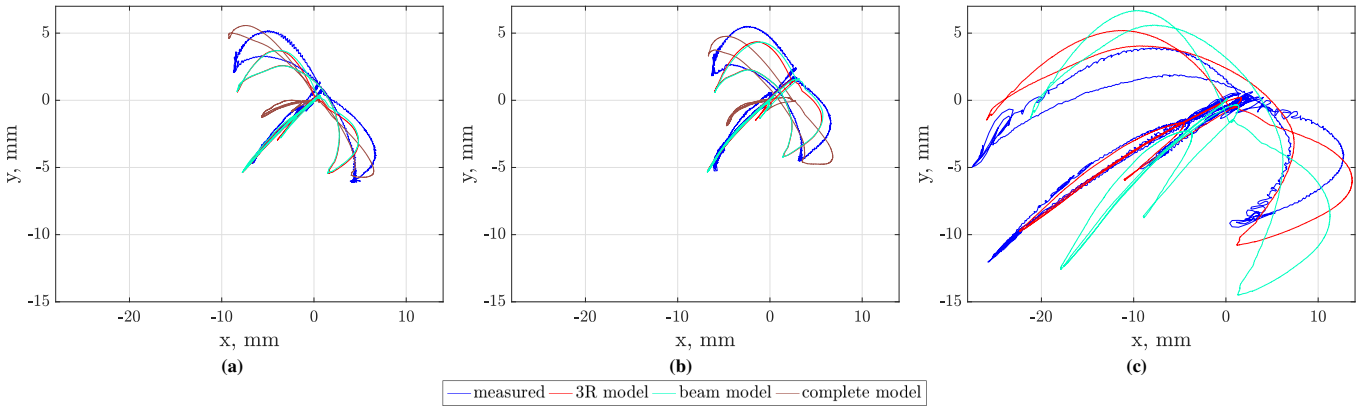

Fig. 6. Mast displacement measurement and simulation: each shroud has a pretension of **(a)** 1200 N and **(b)** 400 N; **(c)** no shrouds

$\mathbf{x}_{\text{be}} = [E\ G]$ and $\mathbf{b}_{\text{be}e} = \delta\mathbf{c}_{i3}$. Once again the $\mathbf{A}_{\text{be}e}$ and $\mathbf{b}_{\text{be}e}$ of each experiment e are concatenated info $\mathbf{A}_{\text{be}}$ and $\mathbf{b}_{\text{be}}$, resp., and the equation $\mathbf{A}_{\text{be}}\mathbf{x}_{\text{be}} = \mathbf{b}_{\text{be}}$ is solved for $\mathbf{x}_{\text{be}}$. We obtained $E_{noshroud} = 6.55e^{10}$ Pa and $E_{1200N} = 1.55e^{11}$ Pa. The identified shear modulus G value was negative, which is not surprising given that in (30) it can be clearly seen that the mast must be under torsion to compute G. Thus the following formula is used: $G = E/(2(1+\nu))$, where for steel the Poisson's ratio is $\nu = 0.3$.

C. Comparison of the mast models

Here the mast displacement is estimated using the three stiffness models and compared with the measured displacement. To estimate the displacement, the following measurements were used: MP pose, cable and shroud tensions. Tests 4, 8 and 10 are shown in Fig. 6. The displacement is shown with respect to the nominal point, which is the C_{13} coordinate when the MP is in the initial pose. Hence $\delta\mathbf{w}_1$ is the difference between the wrench at this initial pose and the wrench computed at every step.

The 3R and beam models give nearly identical results when there is pretension in the shrouds in Figs. 6a and 6b. Indeed, both are estimating perfectly the straight diagonal displacement segment, while not estimating enough amplitude in the wing-like segments. The complete model adds the missing amplitude on the wing-like segments, however the straight segment is estimated with a little skew and overall the estimation appears to be compressed along the diagonal. When comparing the 3R model to the beam model, the only difference can be seen in Fig. 6c, where the shroud model provides a slightly skewed estimation. Overall, all three models estimate trajectories very similar to the measured one. The little differences could be from, for example, identifying shroud elasticity on a short length of 0.5 m instead of the full length, or not modelling the joint clearance at the beam assembly point. Thus, based on these preliminary results, the 3R model could be preferred for further use, as it appears to have the best behavior and is very simple. However, the best evaluation of these models can be done by implementing them in a control scheme such as shown in Fig. 7. In this approach cable anchor points are recomputed at every step, like it is for the pulley model, for example.

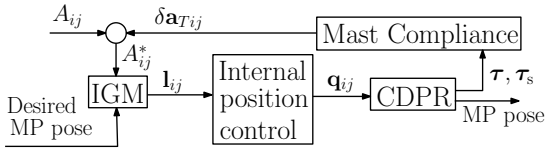

Fig. 7. Control scheme taking into account mast compliance

V. Conclusions

It appears that when designing a deployable CDPR a choice needs to be made whether to favor deployability or accuracy. Indeed, a very compact and lightweight structure may not guarantee a high accuracy due to loss of rigidity. Conversely, a very accurate CDPR cannot be lightweight and easily deployable. However, one can improve the accuracy of a robot by improving the model. The deployable CDPR named Rocaspect has a lightweight structure, consisting of four separate masts. In this paper, the mast top displacement was studied and three models were proposed. The stiffness coefficients for each of the models were identified to then evaluate the models. Overall all models show a promising behavior, while some fine-tuning might be necessary.

It was shown that the amount of pretension greatly affects the mast top coordinates. Indeed, there is a 10 cm difference between the mast coordinates without shrouds and the ones with the highest pretension. On the other hand, mast top displacement during MP trajectory stays under 2 cm given sufficient pretension. Therefore, to improve the accuracy of Rocaspect, shroud length and pretension need to be maintained, preventing changes like shroud creep. This can be done by doing regular tightening of shrouds and measuring their tensions,for example. Once knowledge of nominal coordinates and pretension is ensured, the displacement around the nominal points can be effectively estimated using one of the models.

The future work includes the implementation of the proposed models in the control scheme and evaluation of Rocaspect accuracy.

REFERENCES

[1] A. Pott, H. Mütherich, W. Kraus, V. Schmidt, P. Miermeister, A. Verl, "IPAnema: a family of cable-driven parallel robots for industrial applications", in: *Cable-Driven Parallel Robots (CableCon)*, pp. 119–134, Springer, Stuttgart, Germany, 2012.

[2] M. Gouttefarde, J.-F. Collard, N. Riehl, C. Baradat, "Geometry Selection of a Redundantly Actuated Cable-Suspended Parallel Robot", in: *Transactions on Robotics*, vol. 31 (2), pp. 501–510, IEEE, 2015.

[3] J.-P. Merlet, Y. Papegay, A.-V. Gasc, "The Prince's tears, a large cable-driven parallel robot for an artistic exhibition", in: *International Conference on Robotics and Automation (ICRA)*, pp. 10378–10383, IEEE, Paris, France, 2020.

[4] Z. Zaḳe, N. Pedemonte, B. Moriniere, A. Suarez Roos, S. Caro, "Elasto-Static Model and Accuracy Analysis of a Large Deployable Cable-Driven Parallel Robot", in *Cable-Driven Parallel Robots (CableCon)*, pp. 381–393, Cham: Springer Nature Switzerland, Nantes, France, 2023.

[5] P. Miermeister, M. Lächele, R. Boss, C. Masone, C. Schenk, J. Tesch, M. Kerger, H. Teufel, A. Pott, H. H. Bülthoff, "The cablerobot simulator large scale motion platform based on cable robot technology", in: *International Conference on Intelligent Robots and Systems (IROS)*, pp. 3024–3029, IEEE, Daejeon, Korea, 2016.

[6] W. Kraus, "Force control of cable-driven parallel robots." PhD thesis, Universität Stuttgart, Germany, 2015.

[7] J. B. Izard, A. Dubor, P. E. Hervé, E. Cabay, D. Culla, M. Rodriguez, M. Barrado, "Large-scale 3D printing with cable-driven parallel robots", in: *Construction Robotics*, vol. 1, pp. 69–76, 2017.

[8] L. Gagliardini, "Discrete reconfigurations of cable-driven parallel robots." PhD thesis, École Centrale de Nantes, France, 2016.

[9] Z. Zaḳe, "Design and stability analysis of visual servoing on cable-driven parallel robots for accuracy improvement", PhD thesis, École Centrale de Nantes, France, 2021.

[10] Y. Wu, H. H. Cheng, A. Fingrut, K. Crolla, Y. Yam, D. Lau, "CU-brick cable-driven robot for automated construction of complex brick structures: From simulation to hardware realisation", in: *International Conference on Simulation, Modeling, and Programming for Autonomous Robots (SIMPAR)*, pp. 166–173, IEEE, 2018.

[11] P. Bosscher, R. L. Williams, M. Tummino, "A concept for rapidly-deployable cable robot search and rescue systems", in: *International Design Engineering Technical Conferences and Computers and Information in Engineering Conference*, vol. 47446, pp. 589–598, 2005.

[12] J. P. Merlet, D. Daney, "A portable, modular parallel wire crane for rescue operations", in: *International Conference on Robotics and Automation (ICRA)*, pp. 2834–2839, IEEE, Anchorage, Alaska, USA, 2010.

[13] D. Orbea, C. Cruz, J. Cerro, A. Barrientos, "RUDE-AL: Roped UGV Deployment Algorithm of an MCDPR for Sinkhole Exploration", in *Sensors*, vol. 23, no. 14, pp. 6487, 2023.

[14] Y. Sun, M. Newman, A. Zygielbaum, B. Terry, "Active vibration damping of a cable-driven parallel manipulator using a multirotor system", in: *Cable-Driven Parallel Robots (CableCon)*, pp. 403–414, Springer International Publishing, Krakow, Poland, 2019.

[15] S. Behzadipour, A. Khajepour, "Stiffness of cable-based parallel manipulators with application to stability analysis", in *Journal of Mechanical Design*, vol. 128, no. 1, pp. 303-–310, 2006.

[16] J. Bolboli, M. A. Khosravi, F. Abdollahi, "Stiffness feasible workspace of cable-driven parallel robots with application to optimal design of a planar cable robot", in *Robotics and Autonomous Systems*, vol. 114, pp. 19-–28, 2019.

[17] E. Picard, S. Caro, F. Plestan, F. Claveau, "Stiffness Oriented Tension Distribution Algorithm for Cable-Driven Parallel Robots", in *The 17th International Symposium on Advances in Robot Kinematics*, Ljubljana, Slovenia, 2020.

[18] A. Pott, *Cable-Driven Parallel Robots: Theory and Application*, vol. 120., Springer, 2018.

[19] A. Pott, "Influence of pulley kinematics on cable-driven parallel robots", in: *Latest Advances in Robot Kinematics*, pp 197–204, Springer, Dordrecht, 2012.

[20] E. Picard, S. Caro, F. Claveau, F. Plestan, "Pulleys and Force Sensors Influence on Payload Estimation of Cable-Driven Parallel Robots", in: *Intelligent Robots and Systems (IROS)*, pp. 1429–1436, IEEE, Madrid, Spain, 2018.

[21] T. Paty, N. Binaud, S. Caro, S. Segonds, "Cable-Driven Parallel Robot Modelling Considering Pulley Kinematics and Cable Elasticity", in: *Mechanism and Machine Theory*, art. 104263, vol. 159, 2021.

[22] O. A. Bauchau, J. I. Craig, "Euler-Bernoulli beam theory", in: *Structural analysis*, pp. 173–221, Dordrecht: Springer Netherlands, 2009.

[23] S. Caro, D. Chablat, R. Ur-Rehman, P. Wenger, "Multiobjective design optimization of 3–prr planar parallel manipulators", in: *Global Product Development: Proceedings of the 20th CIRP Design Conference*, pp. 373–383, Springer Berlin Heidelberg, 2011.

[24] A. Pashkevich, D. Chablat, P. Wenger, "Stiffness analysis of overconstrained parallel manipulators", in: *Mechanism and Machine Theory*, vol. 44, no. 5, pp. 966–982, 2009.

[25] P. Miermeister, W. Kraus, T. Lan, A. Pott, "An Elastic Cable Model for Cable-Driven Parallel Robots Including Hysteresis Effects", in *Cable-Driven Parallel Robots (CableCon)*, pp. 17–28, Springer International Publishing, Duisburg, Germany, 2014.

[26] S. Baklouti, E. Courteille, S. Caro, M. Dkhil, "Dynamic and Oscillatory Motions of Cable-Driven Parallel Robots Based on a Nonlinear Cable Tension Model", in *Journal of Mechanisms and Robotics*, vol. 9, no. 6, pp. 1–14, 2017.